AIAA Journal
Vol. 44, No. 12, December 2006

Experimental Investigation of Separation Control Part 1: Baseline and Steady Suction

David Greenblatt,[*] Keith B. Paschal,[†] Chung-Sheng Yao,[‡] Jerome Harris,[§]
Norman W. Schaeffler,[‖] and Anthony E. Washburn[¶]
NASA Langley Research Center, Hampton, Virginia 23681-2199

DOI: 10.2514/1.13817

Low-speed flow separation over a wall-mounted hump, and its control using steady suction, were studied experimentally in order to generate a data set for the development and evaluation of computational methods. The baseline and controlled data sets comprised time-mean and unsteady surface pressure measurements, flowfield measurements using particle image velocimetry, and wall shear stress obtained via oil-film interferometry. In addition to the specific test cases studied, surface pressures for a wide variety of conditions were acquired for different Reynolds numbers and suction rates. Stereoscopic particle image velocimetry and oil-film flow visualization indicated that the baseline time-averaged separated flowfield was two-dimensional. With the application of control, mild three-dimensionality was evident in the spanwise variation of pressure recovery, reattachment location, and spanwise pressure fluctuations.

Nomenclature

A = projected model area, $s \times c$
C_{dp} = form drag coefficient
C_f = wall shear stress coefficient
C_Q = mass-flow coefficient, $Q/U_\infty A$
C_P = time-mean pressure coefficient
C'_P = rms pressure coefficient
C_μ = momentum coefficient, $\dot{m}u_s/qA$
c = model chord length
f = frequency
H = distance between model base and tunnel ceiling
h = model height
k = acceleration parameter, $-(\nu/\rho U_\infty^3)/dp/dx$
M = Mach number
$\dot{m}$ = suction mass-flow rate
Q = suction flow rate
q = freestream dynamic pressure
Re = Reynolds number based on model chord length
Re_θ = Reynolds number based on momentum thickness
s = model span
U, V, W = mean velocities in directions x, y, z
U_∞ = freestream velocity
u, v, w = fluctuating velocities in directions x, y, z
u_s = slot suction velocity
X_B = separation bubble length
x, y, z = coordinate directions measured from the model leading edge
δ = boundary layer thickness
θ = boundary layer momentum thickness

I. Introduction

Boundary layer separation has long been the subject of extensive research due to its prevalence on wings, rotors, compressor blades, and diffusers. Detailed studies have been made of separation from smooth walls [1–3], but for the vast majority of investigations the separation point is fixed (e.g., backward facing steps [4,5], blunt plates or cylinders [6,7], and fences [8]) with reattachment and recovery downstream. The sensitivity of the separated region, or bubble, to upstream conditions depends to a large degree on the geometry used [4,9]. An analysis of low-speed reattachment data showed pressure fluctuation peaks near the reattachment line, with $0.5 \leq fX_B/U_\infty \leq 0.8$ [10]. It has been suggested that such flows are characterized by both the Kelvin–Helmoltz instability of the free shear layer as well as a shedding-type instability of the entire bubble [7,11], or a self-excited flow maintained by a feedback loop [12]. However, at higher Reynolds numbers, typical of flight, this dominant shedding frequency diminishes [13]. With the advent and prevalence of CFD, a large number of computational approaches and turbulence models have become available. A widely accepted approach is to validate methods by comparing predictions with reliable experimental data sets. Progress has been made primarily by studying separation over nominally two-dimensional or axisymmetric geometries. Two classic examples are the incompressible flow over a backward facing step [14,15] and the transonic flow negotiating an axisymmetric bump [16].

The reemergence of active flow control as a technology with potential application in aerodynamics has spawned an urgent need to develop CFD methods with a predictive capability. In the context of separation, the introduction of periodic disturbances is known to exert control over a wide variety of aerodynamic flows. Control is particularly effective when applied in a nominally two-dimensional manner, for example, at the leading edge of a wing or at the shoulder of a deflected flap [17]. Despite intuitive understanding of the flow, at present there is no accepted theoretical model that can adequately explain or describe the observed effects of the leading parameters such as reduced frequency and momentum input. This difficulty stems partly from the superposition of coherent structures and

---

Presented as Paper 2220 at the 2nd AIAA Flow Control Conference, Portland, OR, 28 June–1 July 2004; received 5 October 2004; revision received 3 January 2006; accepted for publication 7 February 2006.

[*] NRC Research Associate, Flow Physics & Control Branch, Mail Stop 170; currently Research Scientist, Hermann Foettinger Institute for Fluid Mechanics, Technical University of Berlin, 8 Mueller Breslau Street, D-10623, Berlin, Germany; david.greenblatt@pi.tu-berlin.de. Senior Member AIAA.

[†] Aerospace Engineer, Flow Physics & Control Branch, Mail Stop 170. Member AIAA.

[‡] Aerospace Engineer, Flow Physics & Control Branch, Mail Stop 170.

[§] Optical Engineering Technician, Flow Physics & Control Branch, Mail Stop 170.

[‖] Research Scientist, Flow Physics & Control Branch, Mail Stop 170. Member AIAA.

[¶] Branch Head, Flow Physics & Control Branch, Mail Stop 170. Senior Member AIAA.

incoherent turbulence where the former are usually driven by at least one instability mechanism.

The development of CFD methods that are meaningful for active flow control applications requires a model geometry that is in some way representative of an aerodynamic body. This generally rules out geometries with fixed separation points discussed earlier. Furthermore, a complete data set (i.e., steady and unsteady surface pressures, two- or three-dimensional velocity and turbulence measurements, and independent skin friction estimates) together with inflow boundary conditions, should be available. Finally, there should be a mechanism in place for effective control of the flow. Because existing data sets did not fulfill all of these requirements, a decision was made to conduct an experimental investigation of a low-speed separated flow that could be subjected to active separation control. The investigation formed part of a CFD validation workshop sponsored jointly by NASA Langley Research Center, the European Research Community on Flow, Turbulence, and Combustion, the U.S. Air Force Office of Scientific Research, the International Association of Hydraulic Engineering and Research, QNET-CFD, and the National Institute of Aerospace. The purpose of this workshop was to bring together an international group of computational fluid dynamics practitioners to assess the current capabilities of different classes of turbulent flow solution methodologies for predicting flow fields induced by zero mass-flux oscillatory jets. A summary of the pertinent workshop computations can be found in [18], where the present case was referred to as "case 3."

The present investigation involved a wall-mounted hump model that was originally designed for, and tested in, a cryogenic pressurized facility [19]. The model was selected because the separated flowfield is effectively insensitive to Reynolds number ($2.4 \times 10^6 \leq Re \leq 26 \times 10^6$) and inflow conditions, and a detailed surface pressure data base already exists. In addition, the resulting separated flow is amenable and responsive to active control via steady suction or blowing as well as zero mass-flux oscillatory blowing. The primary objective of this investigation was to provide a complete data set that could readily be used for the development and evaluation of computational methods. Flow control problems are unique in the sense that they generally involve a so-called baseline state where no control is applied and a controlled state where the active flow control method is applied. Thus, accurate separation control prediction must be preceded by adequate prediction of the baseline state. In an attempt to address this dichotomy, the baseline case was approached as a test case itself, with the generally accepted measurements of surface pressures, flowfield, and wall shear stress.

For the application of active flow control, a graded approach was adopted with a view to assisting the development and evaluation of computational methods. This involved the application of separation control via steady suction before the application of zero mass-flux oscillatory blowing. Both suction and oscillatory blowing were introduced in a nominally two-dimensional manner. Steady suction was achieved via a vacuum pump, whereas zero mass-flux oscillatory blowing was achieved by means of a specially designed actuator. The present paper (Part 1) reports on the data acquired for the baseline case and on the data acquired for control by means of steady suction. Data acquired under the conditions of oscillatory blowing are described fully in Part 2 of this paper [20].

II. Scope & Layout

The model and wind tunnel installation are fully described in Sec. III and compared with the high Reynolds number setup of [19]. Section IV describes the main measurement techniques employed as well as their associated errors. Section V describes the different test cases and the rationale behind their selection. This is followed by the presentation of the main experimental data and is divided into a description of the baseline data (Sec. VI) and the steady suction separation control data (Sec. VII). The paper closes with a summary of the main findings, followed by a brief overview of the oscillatory blowing case (Sec. VIII) that is described fully in Part 2 [20].

III. Experimental Setup

The experiment was performed on a wall-mounted modified Glauert hump model [19], consisting of a relatively long forebody and a relatively short concave ramp comprising the aft part of the model (Fig. 1). A two-dimensional (2-D) slot located at $x/c \approx 0.65$ that led to an interior plenum spanned the model between the forebody and ramp. The model was constructed from aluminum, with the exception of a stainless steel slot upper-lip section. The leading and trailing edges were faired smoothly with a splitter-plate (Figs. 1 and 2), and the model was mounted between two end plates with aluminum frames and glass interiors (Fig. 2). The experiments were performed in the open-return NASA Langley shear flow tunnel with test section dimensions 508 mm (height) and 711 mm (width). The flow was nominally two-dimensional, with sidewall effects (three-dimensional flow) expected near the end plates. The characteristic reference chord length of the model was defined as the length of the hump on the wall, i.e., $c = 420$ mm and its maximum thickness is $h = 53:7$ mm. The model was 584 mm wide and side-mounted end plates were each approximately 235 mm high and 864 mm long. Before installing the model, it was subjected to a detailed quality and assurance regimen where body coordinates were measured along multiple spanwise and chordwise cuts. Maximum spanwise variations in surface geometry over the central half of the model were 35μm (0.00825% of chord). Spanwise slot-width measurements showed an asymmetry that varied from 0.79 to 0.74 mm from left to right (looking upstream). A suction manifold was attached to the plenum that connected to a vacuum pump ($Q_{\max} = 66$ l/s) via heavy-gauge flexible tubing. The suction mass-flow rate was determined by $\dot{m} = \rho Q$, where the air density ρ was calculated from the delivery pressure and temperature, and the suction flow rate Q was measured directly by means of a turbine flowmeter. The main source of error was due to the turbine meter, where $\Delta\dot{m}/\dot{m} \approx \Delta Q/Q \leq 2\%$. Consequently, $\Delta C_Q/C_Q \leq 2\%$ and $\Delta C_\mu/C_\mu \leq 4\%$.

The model was mounted on a splitter-plate (12.7 mm thick), yielding a nominal test section height $H = 382$ mm (i.e., the distance from the splitter-plate to the tunnel ceiling). The ceiling was instrumented along its entire length with 30 pressure ports. The splitter-plate extended 1935 mm upstream of the model's leading edge. The trailing edge of the splitter-plate, which was 1129 mm downstream of the model's leading edge, was equipped with a flap (95 mm long),

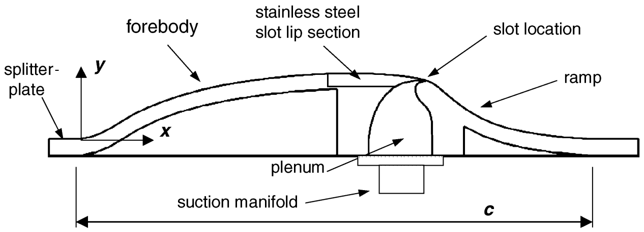

Fig. 1 Cross section schematic through the model showing its various components and the coordinate system used (endplates not shown).

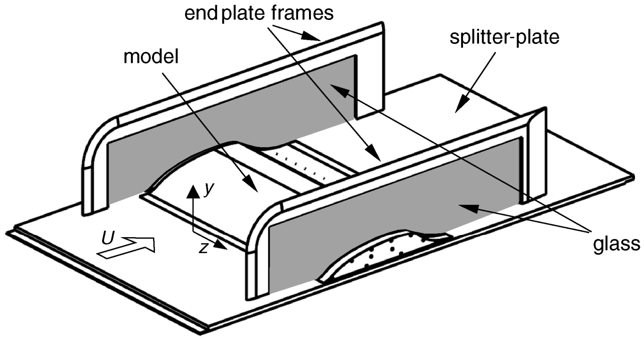

Fig. 2 Isometric view showing the model mounted on the splitter-plate with endplates in place.

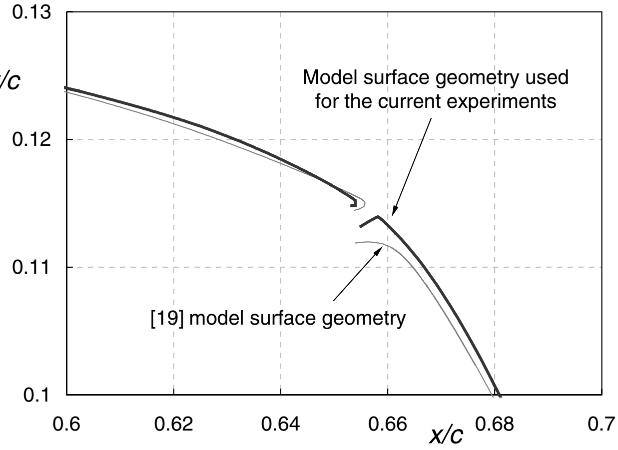

Fig. 3 Comparison of measured model geometries in the vicinity of the slot for present model with [19].

that was deflected 24 deg upwards to reduce circulation around the splitter-plate and avoid separation at the leading edge. The boundary layer was tripped at the splitter-plate leading edge (#60 grit), resulting in a fully developed turbulent boundary layer ($\delta/h \approx 0.57$) at 2.14 chord lengths upstream of the model leading edge, i.e., the "inflow" condition. The tunnel medium was air at sea level.

The present model was designed to be geometrically similar to that of [19] and physically larger by a factor of 2. A comparison of the *measured* centerline surface geometry, nondimensionalized with respect to c for both models, showed a difference in model height of 1%. The models differed mainly with respect to their slot geometries; the present slot width is smaller relative to the chord and has a sharper downstream edge (see Fig. 3). The installations differed in that the present model was mounted on a splitter-plate, whereas that of [19] was mounted on the tunnel floor. The suction manifold and pressure tubing introduced partial blockage on the lower side of the splitter-plate, resulting in net circulation around the splitter-plate. This was ameliorated by means of the trailing-edge flap. Furthermore, the relative height of the model to the test section height differed by a factor of about 1.6. Finally, the Reynolds number ranges were substantially different, with that of the present investigation being typically 20 times smaller (see Table 1).

IV. Measurement Techniques & Accuracy

The model was equipped with 153 centerspan static surface pressure ports (0.5 mm diam) and 20 unsteady surface pressure ports. The unsteady pressure transducers were located 1 mm below the surface, flush mounted against 0.25 mm diam orifices, in the vicinity of the separated flow region (Figs. 4a and 4b). Sixteen spanwise pressure ports were located on the forebody at $x/c = 0.19$ and on the ramp at $x/c = 0.86$ (Fig. 4b). An array of electret-type microphones was also mounted in the separated flow region, but data acquired from these are not reported in this paper. Two-dimensional particle image velocimetry (PIV) data were acquired in a plane, along the model centerline and normal to the surface, from the vicinity just upstream of the slot to well beyond the reattachment location at $x/c \approx 1.4$ (Fig. 4a). Stereoscopic PIV (three-dimensional) data were acquired in planes perpendicular to the flow direction, arranged to intersect the 2-D plane at $x/c = 0.7$ to 1.3 in steps of approximately 0.1. For the baseline case, oil-film interferometry was used to quantify the skin friction over the entire model, from the region upstream of the hump to beyond the reattachment location. Oil-film interferometry was also used for flow visualization in the reattachment region (further details can be found in [21]). For all measurement techniques, bias and precision errors (based on 95% confidence intervals) were estimated (see Table 2) [22,23]. At the inflow location $x/c = -2.14$, pitot-tube and hot-wire anemometer data were compared with 2-D and three-dimensional (3-D) PIV. Inflow skin friction was also documented using oil-film interferometry.

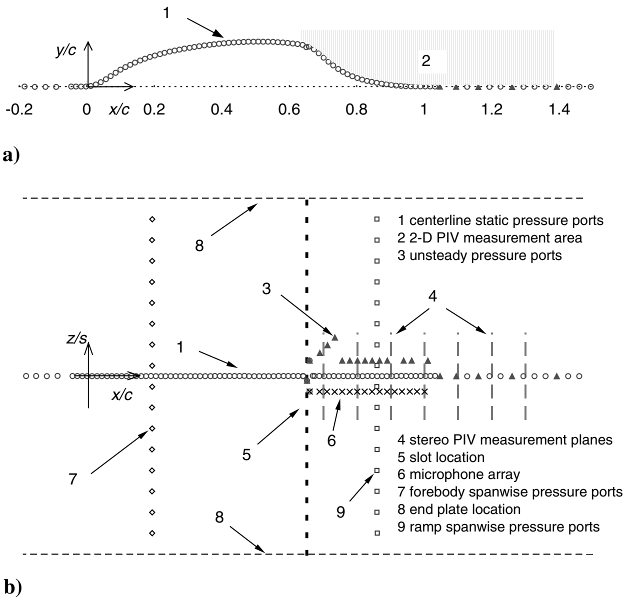

Fig. 4 Schematics showing a) the centerline layout of the pressure ports and 2-D PIV measurement locations, and b) the spanwise distribution of pressure ports and 3-D PIV measurement locations.

A. Mean & Unsteady Surface Pressures

A high-speed pressure scanner, in conjunction with 254 mm water column scanning modules, was used for all mean pressure measurements. Where possible, instrumentation was stowed under the hollow forebody and ramp sections of the model to minimize blockage under the splitter-plate (see Fig. 1). Unsteady pressure measurements were made by means of 20 miniature piezoresistive pressure transducers (maximum range: 6.89 kPa). All pressure transducers were calibrated in situ before each run. Typical mean pressures at the test conditions were acquired and averaged over a 60 s time interval ($tU_\infty/c \approx 5000$). Bias and precision errors are shown in Table 2.

B. Flowfield Measurements

The PIV setup included an Nd:YAG double-pulsed 100 mJ laser and two 1024×1280 CCD cameras installed with either 100 or 200 mm Nikon macro lenses depending on the required resolution. Smoke particles (specific gravity 1.022) were generated by means of a standard smoke generator and the largest particles were on the order of 4–5μm as measured by a commercial aerodynamic particle sizer. Data processing was performed using 28×28 pixel interrogation areas corresponding to either 1×1 or 2×2 mm with a 50% overlap. The time delay between image pairs was set to allow a maximum particle displacement of one-third of the interrogation area (typically 9 pixels) and 400–2000 image pairs were acquired at each location. Because of adequate seeding, optical access, and laser power, erroneous vectors were minimized; relative correlation signal strengths

Table 1 Comparison of conditions in the cryogenic facility with those in the present facility

Investigation	Re range, 10^6	M	Inflow δ/h	Inflow Re_θ, 10^3	h/H	Installation
[19]	2.4–2.6	0.25	~0.56 at $x/c = -1.25$	47–149	8%	tunnel floor
Present	0.372–1.115	≤ 0.12	~0.57 at $x/c = -2.14$	7.2	13%	splitter-plate

Table 2 Maximum bias, resolution, and precision error estimates for all measured quantities

Measured quantity	Bias or resolution	Precision
C_p	0.003	0.008
C_p'	0.001	0.001
U/U_∞, V/U_∞	1.3%	1%
W/U_∞	−3%	1%
$\overline{uu}/U_\infty^2$, $\overline{vv}/U_\infty^2$, $\overline{uv}/U_\infty^2$	0.02%	13%, 13%, 17%
C_f	0.00005	

were then used to remove any remaining erroneous vectors. In addition to the error estimates shown in Table 2, the accuracy of both the mean and fluctuation components of 2-D and 3-D PIV velocity measurements was assessed by means of in situ direct comparison at the inflow location. Three-dimensional PIV data were span-averaged over the central half of the measurement area. For the mean flow, PIV data were compared directly to uncorrected pitot-tube data (see Fig. 5). Apart from the region near the wall, where neither the pitot-tube nor the PIV data are reliable, the 2-D PIV measurements varied by no more than 1% when compared with the pitot-tube data. The largest deviations were observed for $y > 10$ mm ($y^+ > 1000$), where pitot-tube errors are negligibly small [24]. This comparison was consistent with the estimated bias and precision errors shown in Table 2. Three-dimensional PIV, however, consistently underpredicted the velocity by approximately 3% of U_∞. This bias was consistent across the measurement area with spanwise variations typically <3% of U_∞. Consequently, 3-D PIV was used to assess spanwise variations in the flow, but the absolute velocities were not relied upon as being sufficiently accurate for the evaluation of computational models.

Particle frequency response plays an important role in the accuracy of turbulent stress measurements. Measurement accuracy was assessed directly by measuring the inflow ($x/c = -2.14$) and reattached ($x/c = 1.3$) $\overline{uu}$ profiles with both PIV and hot-wire anemometer, to estimate whether the seeding particles had a small enough mass to respond to small scale motions in the flow. The data were further analyzed to determine the particle response characteristics [22] as well as to determine an upper frequency limit of the flow in question [25]. The hot-wire spectra were filtered based on a linear model of particle-lag as a function of flow properties, particle size, and applied acceleration [26]. The inflow ($x/c = -2.14$) 2-D PIV data are shown together with the unfiltered and filtered hot-wire data in Fig. 6. These data are consistent with the results of the particle sizer, namely that the main signal producing particle diameters were on the order of 4μm. The inflow 3-D PIV underpredicted the $\overline{uu}$ hot-wire data by as much as 35% (not shown) and, consequently, these data were not relied upon directly for the turbulence statistics. Particle frequency response was not considered to be a significant source of error in the separated and reattaching boundary layer (see comparison at $x/c = 1.3$ in Fig. 6) because the shear layer turbulent energy is contained at lower frequencies than in the thinner attached inflow boundary layer. In this region, measurement resolution and precision errors dominated (see Fig. 6 and a detailed discussion in [27]). The maximum precision error corresponding to the maximum normal stress is shown on the figure, whereas PIV resolution errors become significant at low $\overline{uu}$ (see Table 2).

C. Oil-Film Interferometry

Surface shear stress was measured, and limited flow visualization was performed, on the model surface using oil-film interferometry. The technique is briefly described here, but a full description of the specific methods and challenges can be found in [21]. A thin Mylar sheet, chosen for its reflective properties and ease of application, was placed on the model from upstream of the leading edge to downstream of the reattachment location. Mylar sheets were also placed along the location corresponding approximately to the baseline and suction reattachment lines on the half-span of the model defined by $-0.5 < z/s < 0$. Oil droplets of varying viscosity were placed on the sheet and thinned at a rate proportional to the shear stress acting on them. Light from an extended monochromatic light source reflected from the oil films and model surfaces and was recorded on a digital camera. Shear stress was inferred by measuring the thickness of the oil at a specific time, using interferometry in conjunction with a photogrammetry technique. Surface pressure taps were used to determine the corresponding locations of shear stress on the model.

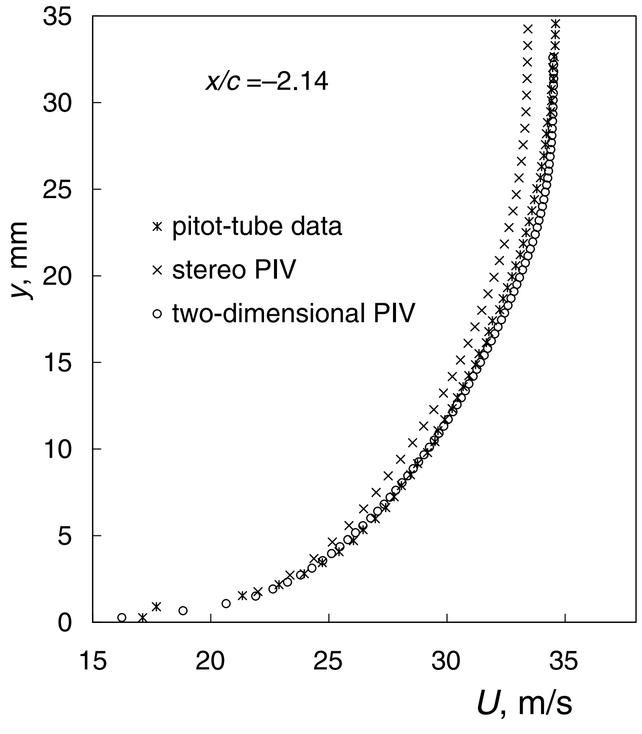

Fig. 5 Inflow mean velocity profile at $x/c = -2.14$ corresponding to the tunnel centerspan.

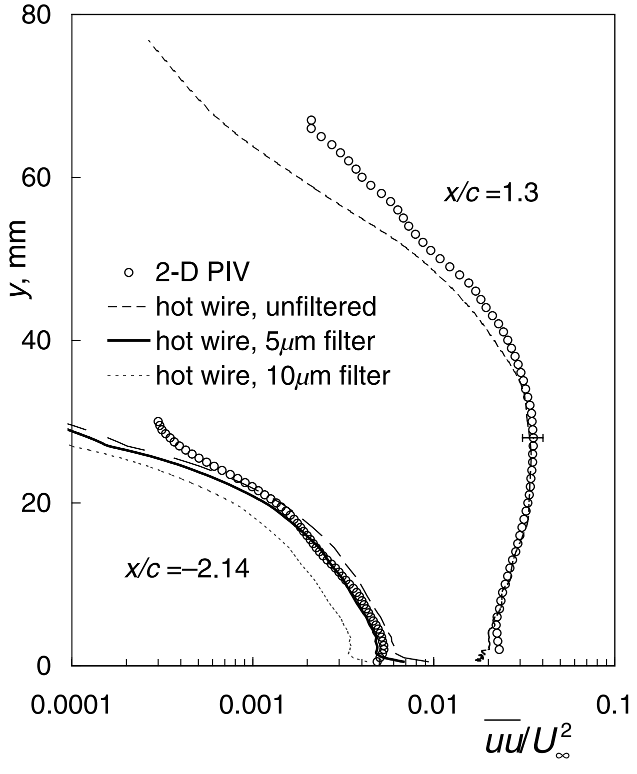

Fig. 6 Inflow and downstream turbulence profile showing sources of 2-D PIV errors.

Because of the spatial averaging method used, maximum bias and precision errors were combined (see [21] and Table 2).

V. Test Cases

Both uncontrolled (baseline) and controlled flow (steady suction) scenarios were considered for approximately $370,000 \leq Re \leq 1.1 \times 10^6$ corresponding to $0.04 \leq M \leq 0.12$; deviations from the nominal Re and M values never varied by more than 1%. One baseline test case ($Re = 929,000$, $M = 0.100$ with no control) and one control test case [$Re = 929,000$, $M = 0.100$, $\dot{m} = 0.01518$ kg/s, corresponding to $C_\mu = 0.24\%$ (or $C_Q = 0.15\%$; see discussion in Sec. VII)] were selected for detailed 2-D and 3-D PIV flowfield measurements. The control test case was chosen to exert substantial control over the separation region, without entirely eliminating the bubble. Elimination of the bubble was not considered desirable for the control test case as this approximates an inviscid flow and would not be appropriate for evaluating the prediction methods. Furthermore, the test case was chosen to correspond to control previously performed under identical nondimensional conditions at high Reynolds numbers [19].

Although a single baseline and a single control test case were selected, mean and unsteady surface pressure data were acquired for a wide variety of conditions, most notably different slot suction rates and Reynolds numbers. A number of dimensionless suction rates at various Reynolds numbers were chosen to correspond to those of ref. [19]. The purpose was to evaluate the effect of Reynolds number and provide additional data for those wishing to conduct sensitivity studies such as, for example, studying the effect of increasing or decreasing the suction rate from the test condition.

VI. Baseline Flow

A. Preliminary Considerations

A general description of the flow is provided with respect to Fig. 7a which shows mean and rms surface pressure coefficients for two scenarios. Mean pressures from all pressure transducers are shown. Flow approaching the model leading edge decelerates but does not separate. Immediately downstream of the leading edge, the boundary layer is subjected to a strong favorable pressure gradient ($k > 3.0 \times 10^{-6}$ for $0.05 < x/c < 0.1$). The pressure gradient then relaxes over the region of the forebody defined approximately by $0.1 < x/c < 0.5$. A C_p anomaly can be seen at $x/c \approx 0.48$ as a result of a 5μm step (0.0012% with respect to chord) at the joint ($x/c = 0.472$) between the aluminum forebody and the stainless steel upper-lip section. At $x/c \approx 0.6$ in the region of strong convex curvature, the pressure increases abruptly and separation occurs at $x/c \approx 0.665$ (determined by surface C_p and 2-D PIV; see Fig. 7b and Table 3). The flow remains separated over the relatively short concave ramp in the aft part of the body and reattaches downstream of the trailing edge at $x/c \approx 1.1$ (see Fig. 7c and Table 3). $C'_{p,\max}$, which is often used to estimate the reattachment point, underpredicts

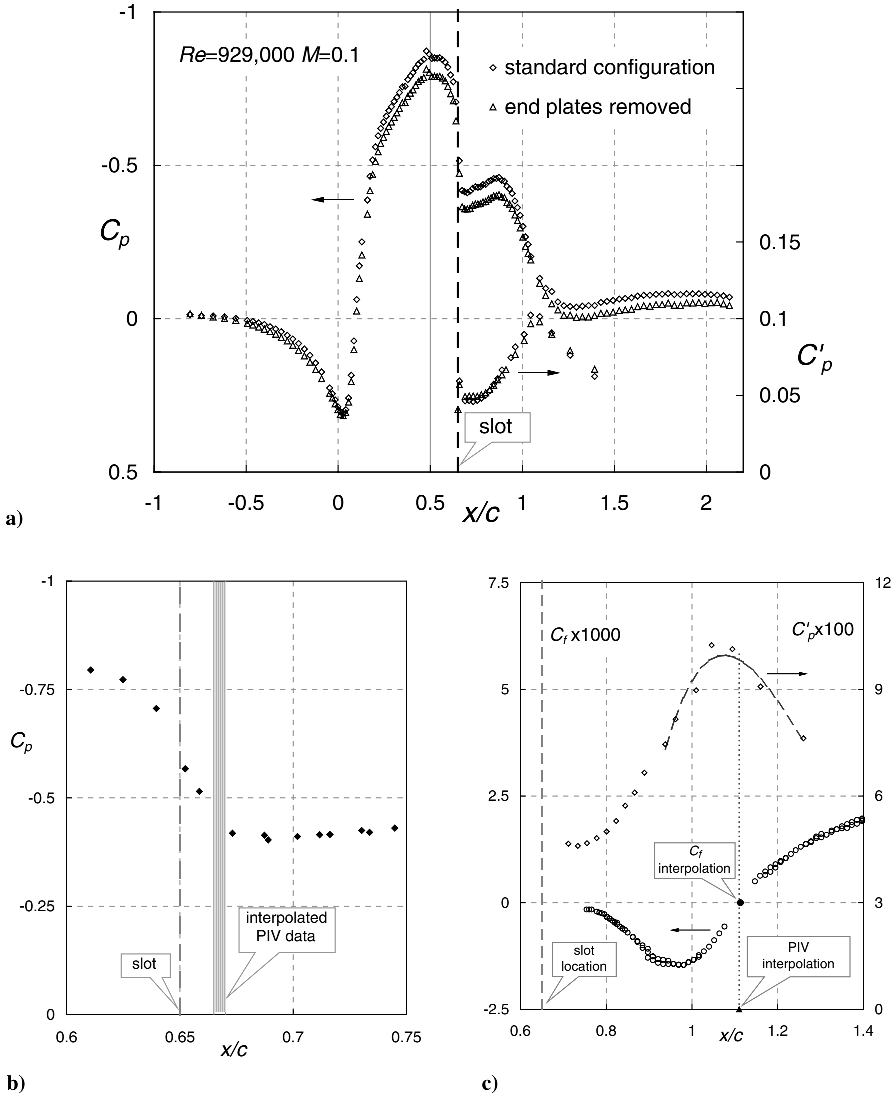

Fig. 7 a) Mean and fluctuating pressures on the model and splitter-plate in its original configuration and with the end plates removed; various methods used for determining b) the flow separation and c) the flow reattachment points.

Table 3 Comparison of measured separation and reattachment location

	Separation measurements	Reattachment measurements & estimates		
Case	2-D PIV Centerline	Oil film (off centerline)	2-D PIV (centerline)	$C'_{p\,\max}$
Baseline	0.665 ± 0.005	1.11 ± 0.003	1.10 ± 0.005	1.08
Control	0.680 ± 0.005	0.94 ± 0.005	0.92 ± 0.005	0.90

it by $x/c \approx 0.003$. Downstream of reattachment, the boundary layer recovers under a near zero pressure gradient. Towards the end of the splitter-plate, the flow decelerates slightly due to the presence of the trailing-edge flap.

Initial surface pressure data were acquired using the original design of the endplates. It was discovered that the aft solid section of the aluminum endplates partially blocked optical access for 3-D PIV measurements. This access problem was somewhat alleviated by shortening the end plate. This modification did not measurably affect the mean and unsteady surface pressure distributions over the entire model. During the course of acquiring data, significant differences were observed between the forebody C_p data and that predicted by 2-D CFD codes [18]. Data acquired with the end plates temporarily removed revealed that their blockage effect was the source of the discrepancies (Fig. 7a). Nevertheless, the mean and rms pressure distributions show that removing the end plates did not materially affect the separation and reattachment locations.

B. Effect of Reynolds Number & Setup Details

Figure 8 shows the baseline mean and rms surface C_p data, from all pressure ports, in the separated flow region as a function of Reynolds number. The test case for the baseline with no control is indicated on the figure. For $Re \geq 557,400$ there is no significant Reynolds number effect in either the mean or rms quantities. Negligible differences were also observed at $x/c < 0.5$ and $x/c > 1.5$ (not shown). Figure 9 shows C_p data for the present test case compared to the high Reynolds data of [19]. (The reference pressure in [19] was adjusted by 0.266% to match their inflow C_p with the present data.) The C_p data near separation are virtually identical, although the high Reynolds number case has a slightly longer bubble than that of the present case. This small difference is possibly a Reynolds number effect or a facility artifact, but is most probably due to the relatively minor geometry differences in the vicinity of the slot (see Fig. 3). In both instances, the slots are not externally sealed. In addition, there is a notable difference in the minimum C_p (the "suction peak") upstream of the slot, just downstream of $x/c \approx 0.35$. This was assumed to be due to the difference in the ratio of model height to tunnel height for the two cases, namely $h/H = 8\%$ [19] vs 13% (present setup; see Table 1). This assumption was supported by CFD for the two configurations where the suction peak difference was computed as being $\Delta C_p \approx 0.1$ (cf. [18,28]). The general trend in C'_p in the separated and reattaching region is similar for both cases although the absolute values differ by about 30%. The differences are probably due to the Reynolds number disparity or the conditions prevailing downstream of the suction peaks, which act as an effective boundary condition for the separated flows. In addition, the C'_p data presented here and throughout this paper is a combination of fluctuations from the facility as well as the local turbulence corresponding to the bandwidth $0.005 \leq fX_B/U_\infty \leq 27$. Independent unsteady pressure measurements were not made in the test section and thus no distinction could be made between facility and flow contributions. Spectral analysis of the pressure signals in the separated region, as well as hot-wire data in the shear downstream of the bubble, showed no preferred or "shedding" frequency associated with the bubble. This should be contrasted with oscillations associated with low Reynolds number separation bubbles [10–12].

The sensitivity of the separated region to the presence of the control slot was investigated. This was achieved by comparing surface mean and fluctuating pressures for the case of an open slot with the case of a slot taped over externally (tape dimensions 6.4-mm-wide, 64μm-thick) for several Reynolds numbers. In the case of the open slot, the plenum is sealed at the base of the suction manifold. The data presented in Fig. 10 shows that the presence of the slot has a

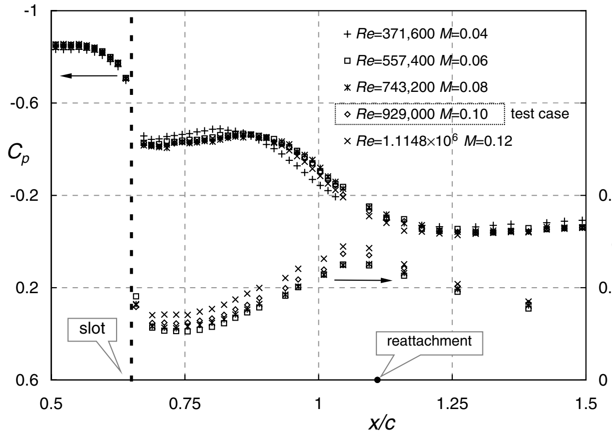

Fig. 8 Effect of Reynolds number on surface pressures including test case Reynolds number.

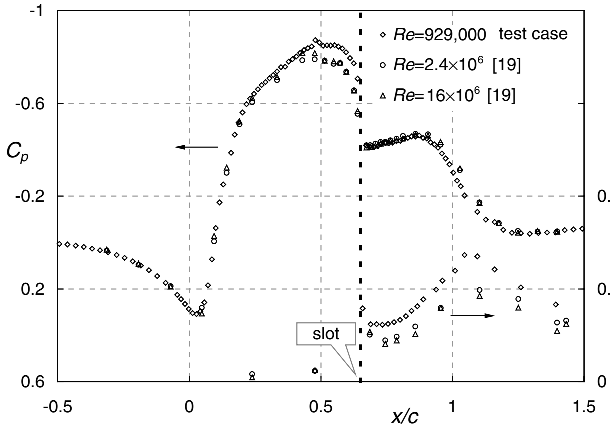

Fig. 9 Comparison of test case surface pressure with [19] at high Reynolds numbers.

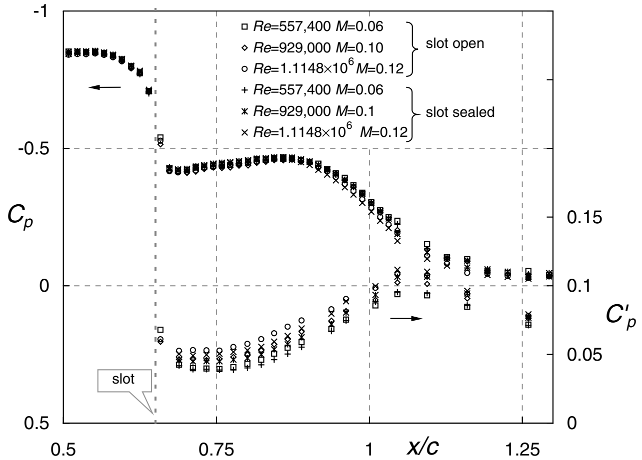

Fig. 10 Effect of the slot on surface pressures for different Reynolds numbers.

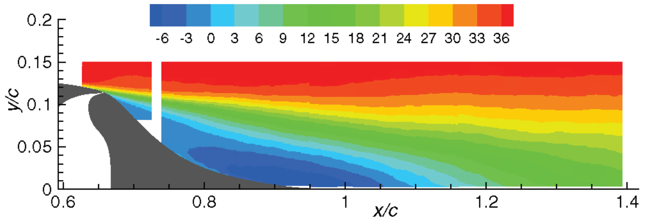

Fig. 11 Superposition of four blocks of 2-D PIV U-component data, m/s.

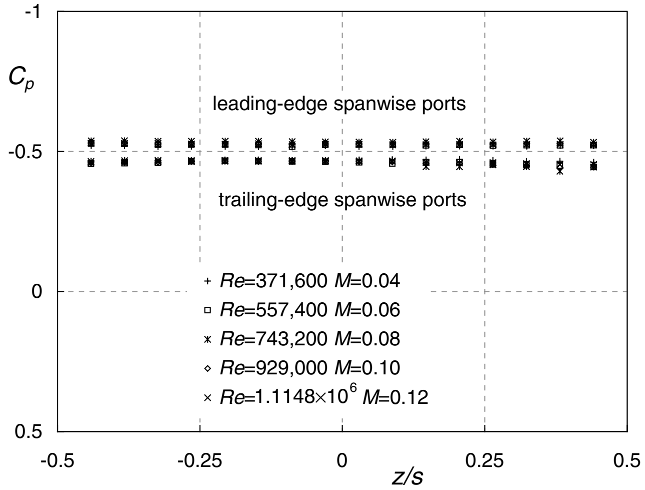

Fig. 12 Spanwise pressure uniformity on the forebody ($x/c = 0.19$) and in the separated region on the ramp ($x/c = 0.86$).

negligible effect on either the mean or the fluctuating pressures. On the basis of this finding, all subsequent flowfield data were acquired with the slot open.

C. Baseline Flowfield & Two-Dimensionality

To map the baseline test case flowfield from upstream of separation ($x/c = 0.62$) to downstream of reattachment ($x/c = 1.4$), the field was divided into four zones, three of which overlapped. A composite plot showing the streamwise velocity contour U is shown in Fig. 11. Velocity components U, V and turbulent stresses $\overline{uu}$, $\overline{vv}$, and $\overline{uv}$ could be extracted from this data at arbitrary x/c for comparison with CFD results. Separation and reattachment points were estimated from this data (see Figs. 7b and 7c and Table 3) where higher resolution data were acquired in the vicinity of the slot.

Flow two-dimensionality in the separated and reattachment region was assessed via three methods: 1) from the spanwise pressures on the ramp in the separated region, 2) by performing 3-D PIV measurements in planes perpendicular to the flow direction, and 3) by means of the surface oil-film flow visualization. Spanwise surface pressures were also measured on the forebody of the model.

Spanwise pressures are shown in Fig. 12 for both forebody ($x/c = 0.19$) and ramp ($x/c = 0.86$) pressure ports at various Reynolds numbers. The spanwise variations are small, e.g., at the test condition, the pressure variation over the central half of the model ($-0.25 \leq z/s \leq 0.25$) is $\Delta C_p = \pm 0.005$. Departures from two-dimensionality are mainly near the end plates. Streamwise velocity components of 3-D PIV data acquired upstream of reattachment, near reattachment, and downstream of reattachment, over 20% of the span, are shown in Figs. 13a–13c respectively. These data show small departures from two-dimensionality and the spanwise variations are on the order of the 3-D PIV accuracy. Maximum in-plane velocities V and W (not shown) were typically 3% of U_∞.

Examples of 2-D and 3-D PIV mean velocity and turbulence profiles, in the vicinity of reattachment, are shown in Figs. 14a–14d and Figs. 14e–14h, respectively. U is the streamwise component and V is the component normal to the splitter-plate. 3-D data are based on a span-average of the center 10% of the model span, comprising 36 individual profiles. The mean velocity data are consistent with the inflow observations discussed in Sec. IV.C, namely that the 3-D PIV underpredicted mean velocity profiles by as much as 3% of the maximum. The main sources of error in the 2-D turbulence measurements were due to bias and precision, with particle response being negligible (cf. Fig. 6). 3-D turbulence measurements showed a vast improvement over the inflow measurements discussed in Sec. IV.B, but were not consistently within the 2-D precision and bias errors.

Several attempts were made at assessing the two-dimensionality of the reattachment line using china clay and microtufts. Neither gave sufficiently good resolution. Consequently, oil-film interferometry was used in the reattachment region, where $C_f \approx 0$, which was determined previously by interpolating wall shear stress data (see Sec. IV.C and Fig. 7c). Hence, reattachment line two-dimensionality was assessed by exploiting the flow visualization attribute of oil-film interferometry. This was achieved by placing oil drops diagonally across a line that extended from the centerline in the negative z-direction and corresponding to the previously measured reattachment x/c location (see Fig. 15). Oil was applied in discrete drops and films were generated using a method similar to that described in [21], with the exception that overlapping images were acquired by traversing the camera in the z-direction along the span of the model. The images were then corrected for perspective and pieced together by matching corresponding fringes from the different images. A composite of the images resulting from this procedure is shown in Fig. 15. The oil-film method clearly can be used as a flow visualization technique as well as yielding quantitative shear stress data.

The composite of images shows that the reattachment line is essentially two-dimensional and, for most films, the downstream and upstream flow directions can be clearly identified. Although the reattachment line is essentially two-dimensional, there appears to be a crossflow component with the shear stress acting perpendicular to the reattachment line at some locations. Note, however, that the shear stress near reattachment is extremely low as can be seen by comparing the fringe spacing near the reattachment line $x/c \approx 1.11$ with that at $x/c = 1.05$ and $x/c = 1.15$, where C_f is higher but still low (approximately -0.001 and 0.001, respectively). Note that, in regions of such low shear stress, the oil film is subject to other forces (e.g., pressure and gravity forces), which can dominate its behavior.

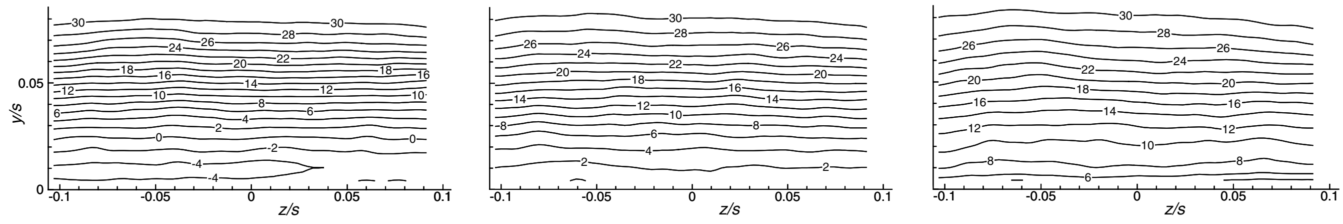

a) $x/c = 1.0$ **b) $x/c = 1.1$** **c) $x/c = 1.2$**

Fig. 13 Baseline 3-D PIV measurements of streamwise velocity U acquired a) upstream of reattachment, b) approximately at reattachment, and c) downstream of reattachment.

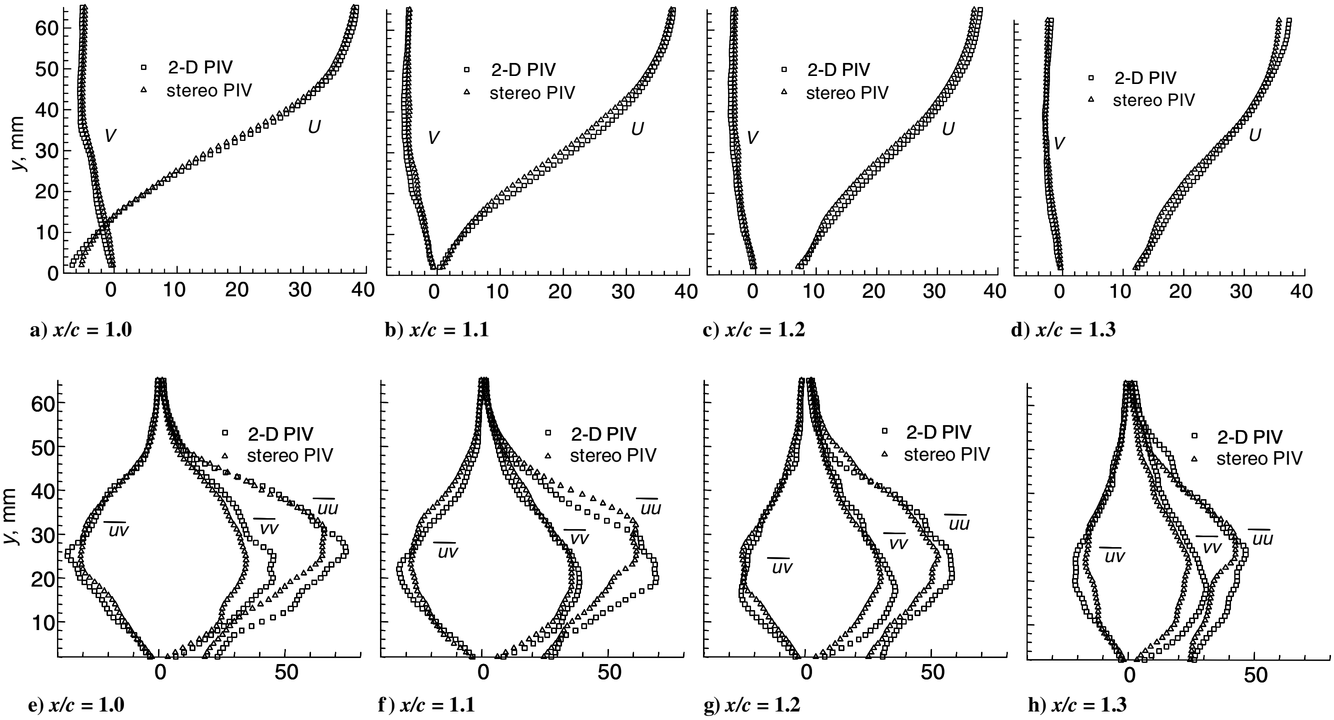

a) *x/c* = 1.0 b) *x/c* = 1.1 c) *x/c* = 1.2 d) *x/c* = 1.3

e) *x/c* = 1.0 f) *x/c* = 1.1 g) *x/c* = 1.2 h) *x/c* = 1.3

Fig. 14 Comparison of 2-D and span-averaged 3-D velocity and turbulence profiles in the vicinity of reattachment for the baseline case.

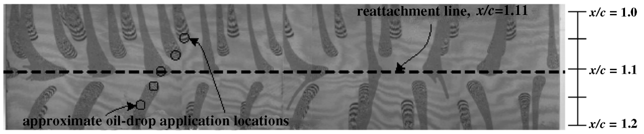

Fig. 15 Oil-film flow visualization over one-half of the model span ($-0.5 < z/s < 0$) near reattachment location for the baseline case.

For some of the oil drops applied on the reattachment line, as well as those close to the end plates, the forces were not large enough to thin the oil sufficiently to generate fringes over the duration of the run.

VII. Control via Steady Suction

For the suction test case, control was applied via the two-dimensional slot using a suction rate of 0.01518 kg/s at $Re = 929,000$. Details of the suction setup and uncertainties are discussed in Secs. III and V. Although not required for the test case, control was applied at various suction rates and for the same dimensionless conditions at different Reynolds numbers. A number of cases were selected to yield the same dimensionless conditions as that of [19]. (Suction rates are often expressed as a mass-flow coefficient [29], presently $C_Q = 0.15\%$. For consistency with [19] and to facilitate direct comparison with oscillatory cases, current data were presented in terms of C_μ.)

A. Effect of Suction Rate & Reynolds Number

The effect of gradually increasing the suction rate from 0 kg/s (baseline) is shown in Fig. 16. Application of suction accelerates the flow upstream of the slot, increases the pressure downstream thereof, and shortens the bubble length. Suction rates less than and greater than the test case C_μ were acquired to allow the option of conducting a sensitivity study. A comparison of pressure data at the test condition is shown for various Reynolds numbers, including that of [19] in Fig. 17. There appears to be a small Reynolds number effect in that control becomes slightly more effective with increasing Reynolds number. This is also consistent with data from [19], despite the differences in control slot design. Additional data were acquired at a higher suction rates (e.g., $C_\mu = 0.47\%$; see Fig. 18) and a similar Reynolds number dependence was observed. However, the disparity between the current data and that of [19] appeared to increase substantially. This apparent Reynolds number effect is discussed further in Sec. VII.C.

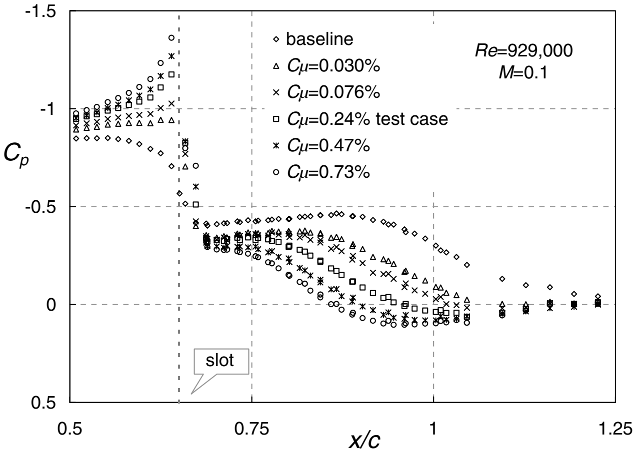

Fig. 16 Effect of separation control via steady suction from the two-dimensional slot, including the control test case.

B. Controlled Flowfield & Two-Dimensionality

The streamwise velocity field for the control test case is shown in the composite plot of Fig. 19. As in the baseline case, the field was divided into four zones, where velocity components U, V, and turbulent stresses $\overline{uu}$, $\overline{vv}$, and $\overline{uv}$ could be extracted from this data at arbitrary x/c for comparison with CFD predictions. Separation and reattachment points were again estimated from this data (see Table 3) and compared with oil-film data.

Spanwise ramp pressures at $x/c = 0.86$ are shown in Fig. 20, which correspond to the cases shown in Fig. 17. For small suction rates $C_\mu = 0.03\%$, the spanwise pressures increase in unison. As the suction flow rate increases further, the pressures appear to develop a mild wavelike distribution with the maximum pressure recovery near the model centerspan and pressure minima at $z/s \approx \pm 0.25$. This

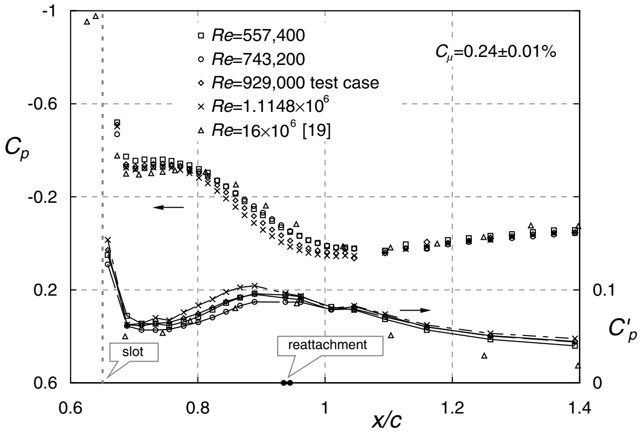

Fig. 17 Effect of Reynolds number on control at the test condition.

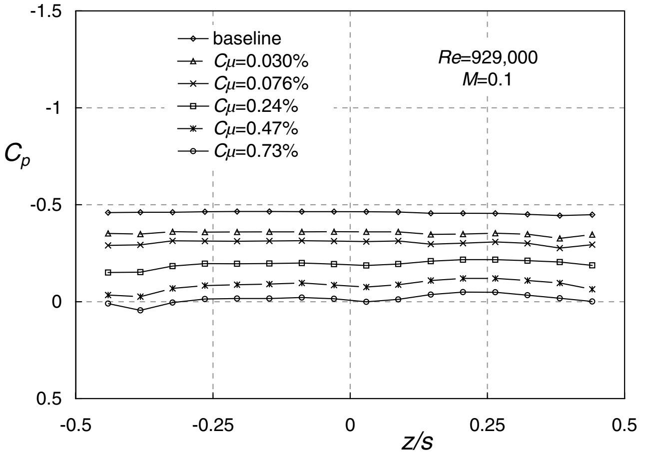

Fig. 20 Effect of increasing suction control on spanwise pressures on the ramp at $x/c = 0.86$.

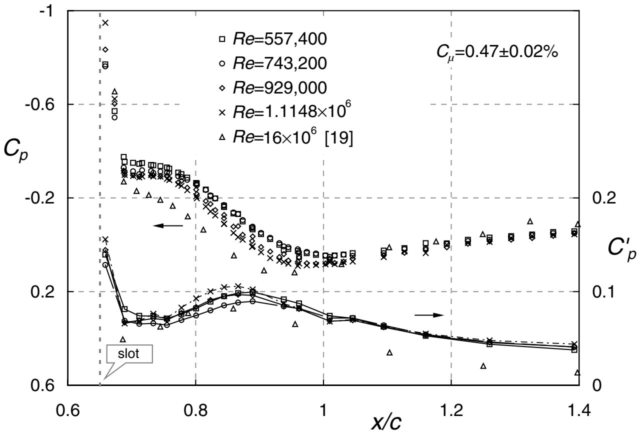

Fig. 18 Effect of Reynolds number on control at a greater suction rate than the test condition.

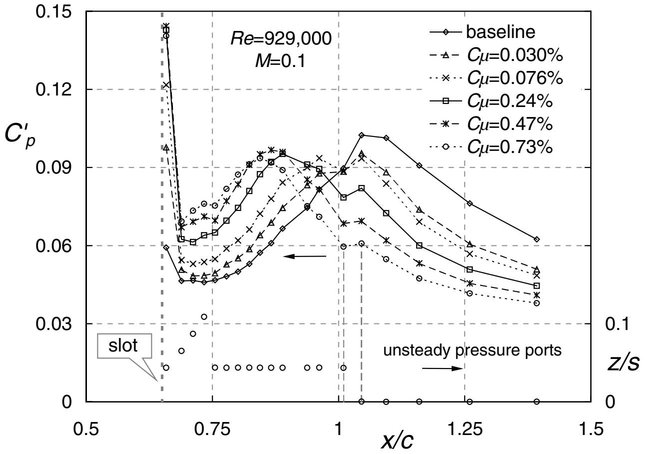

Fig. 21 Effect of increasing suction control on rms pressures in reattachment region.

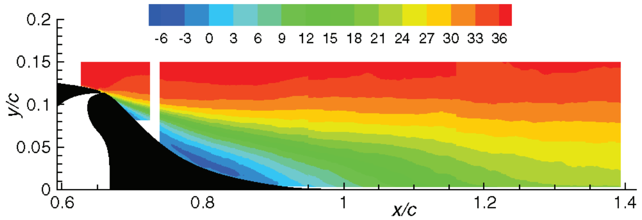

Fig. 19 Superposition of four blocks of 2-D PIV *U*-component data, from upstream of separation to downstream of the reattachment region for the controlled case, m/s.

pressure signature becomes more pronounced with increasing suction rate. Note, furthermore, that the signature is asymmetric, with a larger overall pressure recovery at $z/s < 0$. This is most probably due to the slot-width asymmetry that varies from 0.79 to 0.74 mm from $z/s = -0.5$ to 0.5.

Further evidence of mild three-dimensionality can be seen from the C_p' data shown in Fig. 21. Just beyond $x/c = 1.0$, a small C_p' discontinuity can be seen where the unsteady pressure ports are not aligned along the same spanwise line (shown in the lower part of the figure). Thus, although the static pressures only show negligible variation near the centerspan, there is evidence of mild spanwise variation in the pressure fluctuations. 3-D PIV data of streamwise velocity U near the reattachment location (Fig. 22a), however, did not show significant three-dimensional features, although crossflow velocities $W \approx 0.1U_\infty$ were detected near the wall. Downstream of separation (Figs. 22b and 22c), the flow maintains an essentially two-dimensional character, where the apparent spanwise variation in streamwise velocity is on the order of the 3-D PIV accuracy. Optical blockage as a result of the aft part of the end plate frame precluded 3-D PIV measurements just upstream of reattachment.

As in the baseline case, mean velocity and turbulence profiles for 2-D and 3-D span-averaged data are similar; thus the descriptions and arguments presented in Sec. VI also apply to the control case. For flow visualization, the reattachment location was further up the ramp than for the baseline case and thus oil drops were subject to the effect of gravity. To ameliorate this problem, the oil was applied at different locations for several individual runs, as this allowed a shorter time between applying the films and establishing the test condition U_∞ in the tunnel. The reattachment location was identified as being at $x/c \approx 0.94$ in the region defined by $z/s < 0$ (see Table 3). Consistent with the higher crossflow velocities near the wall, the crossflow shear stress was larger than in the baseline case. Furthermore, 2-D PIV at the centerline showed reattachment to be at $x/c \approx 0.92$, which is consistent with the greater pressure recovery near the centerline (Fig. 20). Thus, three-dimensional effects appear stronger than in the baseline case, but still do not appear to play a dominant role in the flow.

C. Global Features

In addition to the existing cases, it was desired to investigate the global effect of control as well as its effect on the separation bubble. The vacuum pump capacity was insufficient to fully eliminate the bubble (insufficient C_μ) at the test Reynolds number and thus a lower Reynolds number was employed for this purpose. The model form drag coefficient C_{dp} and separation bubble length X_B/c are shown for the two Reynolds numbers in Fig. 23. For the data range shown,

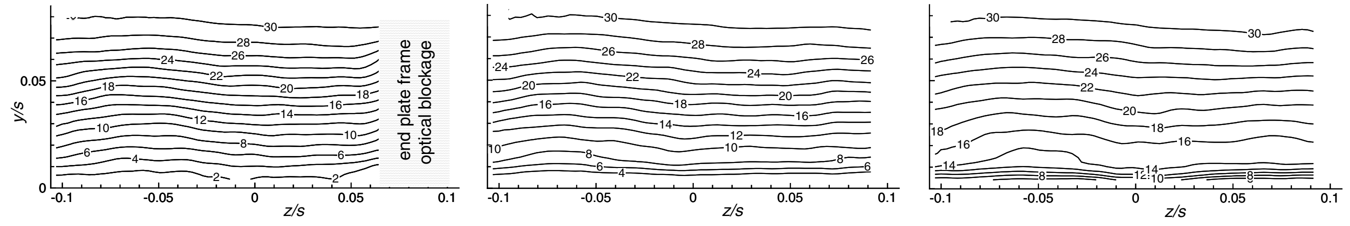

a) ***x/c*** **= 0.95** **b)** ***x/c*** **= 1.0** **c)** ***x/c*** **= 1.1**

Fig. 22 3-D PIV measurements of streamwise velocity *U* acquired near reattachment for controlled test case.

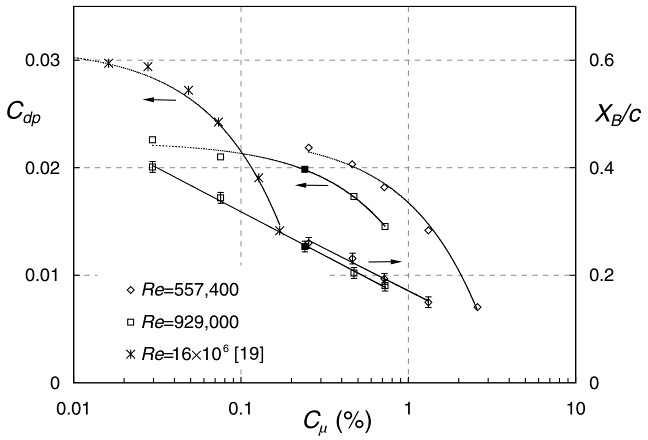

Fig. 23 Form drag coefficient and bubble length as a function of control momentum coefficient (test case has filled symbols).

together with the result of[19], C_{dp} decreases linearly with C_μ and appears to be strongly Reynolds number dependent. This result further elucidates the preceding Reynolds number effect observed. The small geometric and setup differences between the two models (see Sec. III) results in different baseline C_{dp}. Nevertheless, it is evident that "control effectiveness" increases significantly with Reynolds number where $|dC_{dp}/dC_\mu| \propto Re^{0.8}$. The bubble length varies logarithmically with the inverse of C_μ and is not as strongly dependent on Reynolds number. Furthermore, bubble length could not be accurately discerned for $C_\mu > 2$.

VIII. Summary & Future Work

To summarize, it was concluded that the baseline flow was essentially two-dimensional and although minor time-mean three-dimensional features were present, these are not in the form of dominant flow structures. When control was applied, a small but measurable three-dimensional effect was observed. This manifested itself as a mild waviness in the spanwise pressure recovery, variations in spanwise pressure fluctuations, and a small crossflow component identified using oil films and 3-D PIV.

Part 2 of this investigation, involves separation control via zero mass-flux oscillatory blowing introduced from the spanwise slot [20]. This was achieved by means of a rigid piston which was secured to the base of the plenum by means of a flexible membrane. The piston was driven externally by six voice-coil based actuator modules [Aero and Thermally Engineered Actuator Modules (ATEAM) designed and provided by J. Kiedaisch, H. Nagib, and their associates from Illinois Institute of Technology] [30], providing maximum slot velocities of approximately 80 m/s at frequencies ranging from 60 to 500 Hz.

Slot calibration was required to fulfill a number of requirements, such as being experimentally reliable and computationally implementable, being representative of the momentum added to the flow, and maintaining substantial spanwise uniformity (two-dimensionality). Model surface static and dynamic surface pressures were acquired for a wide variety of flow control conditions. At the test condition ($Re = 929,000$, $M = 0.100$, peak slot velocity $=$ 26.6 m/s, and forcing frequency $=$ 138.5 Hz), detailed phase-averaged 2-D and 3-D PIV measurements were made at 36 phases. The peak slot velocity was selected to correspond to a documented high Reynolds number case, [19] as well as the present suction test case slot velocity u_s. Further details of the setup and experimental data can be found in [20].

Acknowledgments

This work was performed while the first author held a National Research Council–NASA Langley Research Center Associateship. The authors wish to thank W. L. Sellers III, M. J. Walsh, L. G. Pack-Melton, M. A. Kegerise, C. L. Rumsey, S. A. Viken, P. Balakumar, A. Seifert (Tel Aviv University), and J. W. Naughton (University of Wyoming) for their many insightful suggestions and comments. The authors also wish to thank R. L. Clark, R. S. Geouge, T. E. Fowler, and M. Bell for their excellent technical support.

References

[1] Simpson, R. L., Chew, Y.-T., and Shivaprasad, B. G., "The Structure of a Separating Turbulent Boundary Layer Part 1: Mean Flow and Reynolds Stresses," *Journal of Fluid Mechanics*, Vol. 113, 1981, pp. 23–51.

[2] Simpson, R. L., Chew, Y.-T., and Shivaprasad, B. G., "The Structure of a Separating Turbulent Boundary Layer Part 2: Higher-Order Turbulence Results," *Journal of Fluid Mechanics*, Vol. 113, 1981, pp. 53–73.

[3] Shiloh, K., Shivaprasad, B. G., and Simpson, R. L., "The Structure of a Separating Turbulent Boundary Layer Part 3: Transverse Velocity Measurements," *Journal of Fluid Mechanics*, Vol. 113, 1981, pp. 75–90.

[4] Eaton J. K., and Johnson, J. P., "A Review of Research on Subsonic Turbulent Flow Reattachment," *AIAA Journal*, Vol. 19, No. 9, 1981, pp. 1093–1100.

[5] Troutt, T. R., Scheelke, B., and Norman, T. R., "Organized Structures in a Reattaching Separated Flowfield," *Journal of Fluid Mechanics*, Vol. 143, 1984, pp. 413–427.

[6] Cherry, N. J, Hillier, R., and Latour, M. E. M., "Unsteady Measurements in a Separated and Reattaching Flow," *Journal of Fluid Mechanics*, Vol. 144, 1984, pp. 13–46.

[7] Sigurdson, L. W., "The Structure and Control of a Turbulent Reattaching Flow," *Journal of Fluid Mechanics*, Vol. 298, 1995, pp. 139–165.

[8] Ruderich, R., and Fernholz, H. H., "An Experimental Investigation of a Turbulent Shear Flow with Separation, Reverse Flow, and Reattachment," *Journal of Fluid Mechanics*, Vol. 163, 1986, pp. 283–322.

[9] Castro, I. P., and Epik, E., "Boundary Layer Development after a Separated Region," *Journal of Fluid Mechanics*, Vol. 374, 1998, pp. 91–116.

[10] Mabey, D. G., "Analysis and Correlation of Data on Pressure Fluctuations in Separated Flow," *Journal of Aircraft*, Vol. 9, No. 9, 1972, pp. 642–645.

[11] Sigurdson L. W., and Roshko, A., "Controlled Unsteady Excitation of a Reattaching Flow," AIAA Paper 85-0552, 1985.

[12] Kiya, M., Shimizu, M., and Mochizuki, O., "Sinusoidal Forcing of a Turbulent Separation Bubble," *Journal of Fluid Mechanics*, Vol. 342, 1997, pp. 119–139.

[13] Seifert, A., and Pack, L. G., "Dynamics of Active Separation Control at High Reynolds Numbers," AIAA Paper 2000-409, 2000.

[14] Driver, D. M., and Seegmiller, H. L., "Features of a Reattaching Turbulent Shear Layer in Divergent Channel Flow," *AIAA Journal*,

Vol. 23, 1985, pp. 163–171.

[15] Yang, J. T., Tsai, B. B., and Tsai, G. L., "Separated-Reattaching Flow over a Backstep with Uniform Normal Mass Bleed," *Journal of Fluids Engineering*, Vol. 116, 1994, pp. 29–35.

[16] Bachalo, W. D., and Johnson, D. A., "Transonic Turbulent Boundary-Layer Separation Generated on an Axisymmetric Flow Model," *AIAA Journal*, Vol. 24, No. 2, 1986, pp. 437–443.

[17] Greenblatt, D., and Wygnanski, I., "Control of Separation by Periodic Excitation," *Progress in Aerospace Sciences*, Vol. 37, No. 7, 2000, pp. 487–545.

[18] Rumsey, C., Gatski, T., Sellers, W., Vatsa, V., and Viken, S., "Summary of the 2004 CFD Validation Workshop on Synthetic Jets and Turbulent Separation Control," AIAA Paper 2004-2217, 2004.

[19] Seifert, A., and Pack, L. G., "Active Flow Separation Control on Wall-Mounted Hump at High Reynolds Numbers," *AIAA Journal*, Vol. 40, No. 7, 2002.

[20] Greenblatt, D., Paschal, K. B., Yao, C. S., and Harris, J., "Experimental Investigation of Separation Control Part 2: Zero Mass-Flux Oscillatory Blowing," *AIAA Journal* (to be published); also AIAA Paper 2005-0485, 2005.

[21] Naughton, J., Viken, S., and Greenblatt, D., "Wall Shear Stress Measurements on the NASA Hump Model for CFD Validation," *AIAA Journal*, Vol. 44, No. 6, June 2006, pp. 1255–1265; also AIAA Paper 2004-2607, 2004.

[22] Coleman, H. W., and Steele, W. G., Jr., *Experimentation and Uncertainty Analysis for Engineers*, Wiley, New York, 1989, Chaps. 2, 3.

[23] Benedict, L. H., and Gould, R. D., "Towards Better Uncertainty Estimates for Turbulence Statistics," *Experiments in Fluids*, Vol. 22, No. 2, 1996, pp. 129–136.

[24] McKeon, B. J., Li, J., Jiang, W., Morrison, J. F., and Smits, A. J., "Pitot Probe Corrections in Fully Developed Turbulent Pipe Flow," *Measurement Science and Technology*, Vol. 14, No. 8, 2003, pp. 1449–1458.

[25] Kistler, A. L., "Fluctuation Measurements in a Supersonic Turbulent Boundary Layer," *Physics of Fluids*, Vol. 2, No. 3, 1959.

[26] Adrian, R. J., "Particle-Imaging Techniques for Experimental Fluid Mechanics," *Annual Review of Fluid Mechanics*, Vol. 23, 1991, pp. 261–304.

[27] Schaeffler, N. W., and Jenkins, L. N., "The Isolated Synthetic Jet in Crossflow: A Benchmark for Flow Control Simulation," AIAA Paper 2004-2219, 2004.

[28] Viken, S., Vatsa, V., Rumsey, C., and Carpenter, M., "Flow Control Analysis on the Hump Model with RANS Tools," AIAA Paper 2003-218, 2003.

[29] Poisson-Quinton, P., and Lepage, L., Survey of French Research on the Control of Boundary Layer and Circulation, *Boundary Layer and Flow Control: Its Principles and Application*, edited by G. V. Lachmann, Vol. 1, Pergamon, New York, 1961, pp. 21–73.

[30] Nagib, H., Kiedaisch, J., Wygnanski, I., Stalker, A., Wood, T., and McVeigh, M., "First-in-Flight Full-Scale Application of Active Flow Control: The XV-15 Tiltrotor Download Reduction," Presented at the Research and Technology Organization AVT-111 Specialists' Meeting on Enhancement of NATO Military Flight Vehicle Performance, Oct. 2004, Paper 29.

T. Beutner
Associate Editor